Supplementary Material: Photo-induced phase transitions in ferroelectrics

Charles Paillard,[1,2] Engin Torun,[3] Ludger Wirtz,[3] Jorge Íñiguez,[4,3] and Laurent Bellaiche[1]

[1] *Department of Physics and Institute for Nanoscience and Engineering, University of Arkansas, Fayetteville, Arkansas 72701, USA*
[2] *Laboratoire Structures, Propriétés et Modélisation des Solides, CentraleSupélec, UMR CNRS 8580, Université Paris-Saclay, 91190 Gif-sur-Yvette, France**
[3] *Physics and Materials Science Research Unit, University of Luxembourg, 162a avenue de la Faïencerie, L-1511 Luxembourg, Luxembourg*
[4] *Materials Research and Technology Department, Luxembourg Institute of Science and Technology (LIST), Avenue des Hauts-Fourneaux 5, L-4362 Esch/Alzette, Luxembourg*

Pattern notation	Space Group
$000/000$	$Pm\bar{3}m$
$000/00w^+$	$P4mm$
$000/0^+v^+v^+$	$Amm2$
$000/u^+u^+u^+$	$R3m$

TABLE I. Correspondence between pattern notation used in the main manuscript and space group for BTO.

BRILLOUIN ZONE

The notation of the high symmetry point in the Brillouin zone of the cubic $Pm\bar{3}m$ phase is taken as follows: $\Gamma = (0,0,0)$, $X = (1/2,0,0)$, $M = (1/2,1/2,0)$ and $R = (1/2,1/2,1/2)$.

ATOMIC DISPLACEMENTS

BTO

BTO is a classical ferroelectric which exhibits a transition from a centrosymmetric cubic $Pm\bar{3}m$ phase to a ferroelectric tetragonal $P4mm$ below ∼393 K with polarization along the tetragonal axis [001], then to an orthorhombic structure $Amm2$ with polarization along a $< 101 >$ pseudocubic direction below ∼280-270 K and finally to a rhombohedral $R3m$ phase with polarization along a $< 111 >$ pseudocubic direction below ∼183 K [1, 2].

In the main manuscript, we refer to those phases with respect to their dipolar and oxygen octahedra tilt pattern. The correspondence between the space group and pattern notation can be found in Table I

Moreover, the polar phase $P4mm$ atomic positions are [2]

- Ba $(0,0,0)$
- Ti $(1/2,1/2,1/2+\delta_{Ti})$
- Equatorial oxygens O, $(1/2,0,1/2+\delta_{O_1})$ and $(0,1/2,1/2+\delta_{O_1})$
- Apical oxygen O, $(1/2,1/2,\delta_{O_3})$

In the $Amm2$ orthorhombic phase, the atoms have the following positions in pseudocubic axes:

- Ba $(0,0,0)$
- Ti $(1/2+\delta_{Ti},1/2-\delta_{Ti},1/2)$
- Oxygens O, $(\delta_{O_1,1},1/2-\delta_{O_1,2},1/2)$ and $(1/2+\delta_{O_1,2},-\delta_{O_1,1},1/2)$.
- Apical oxygen O, $(1/2+\delta_{O_3},1/2-\delta_{O_3},0)$

The rhombohedral $R3m$ phase is characterized by the displacement pattern:

- Ba $(0,0,0)$
- Ti $(1/2+\delta_{Ti},1/2+\delta_{Ti},1/2+\delta_{Ti})$
- Oxygens O, $(\delta_{O_3},1/2+\delta_{O_1},1/2+\delta_{O_1})$, $(1/2+\delta_{O_1},\delta_{O_3},1/2+\delta_{O_1})$, and $(1/2+\delta_{O_1},1/2+\delta_{O_1},\delta_{O_3})$

The displacement pattern for those three phases is plotted in Fig. (1) as a function of the n_{ph} photocarrier density, and shows the disappearance of any polar displacement in all three phases at around $n_{ph} = 0.1$ e/f.u. The resulting phase is the cubic paraelectric $Pm\bar{3}m$ state.

PTO

In Table II, we give the correspondence between the different pattern notations employed and the space group considered in the case of PTO.

In Fig. (2), we plot the displacement of atoms in PTO. The upper panel of Fig. (2) shows the displacement of the Ti, equatorial O_1 atoms and apical O_3 atom of the tetragonal $P4mm$ phase. One can observe that, unlike the case of BTO, the polar displacement (PD) remains relatively robust against the increase of photo-excited carrier concentration. The middle panel depicts the displacement of Ti and O atoms projected on the [111] pseudocubic direction of the rhombohedral $R3c$ cell, showing that it decays into a $R\bar{3}c$ phase with no PD. At last, in the lower panel

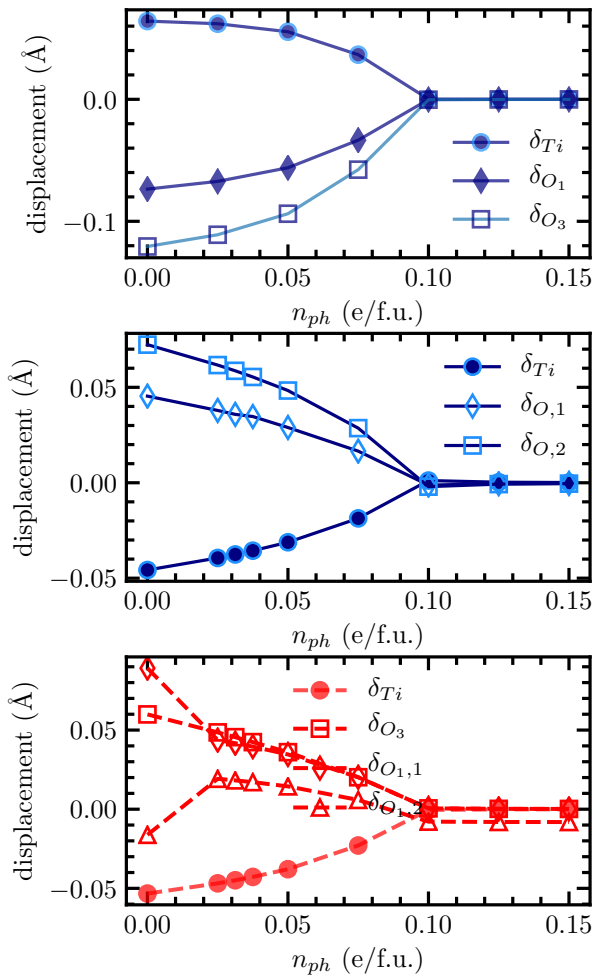

FIG. 1. Displacement pattern (top panel) for the $P4mm$ phase, (middle panel) the $R3m$ phase and (lower panel) the $Amm2$ phase in $BaTiO_3$.

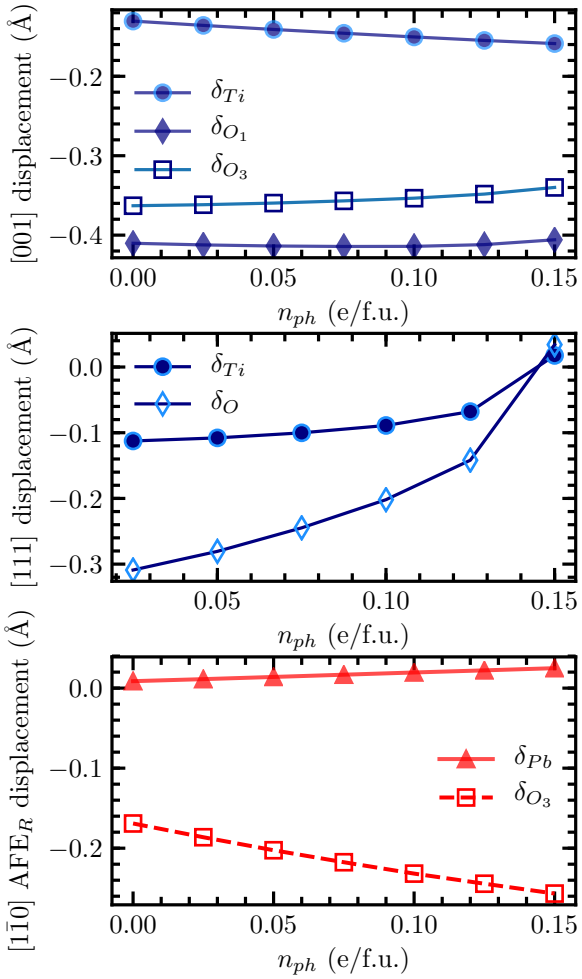

FIG. 2. Displacement pattern (top panel) for the $P4mm$ phase, (middle panel) the $R3c$ phase and (lower panel) the $Imma$ phase in $PbTiO_3$.

Pattern notation	Space Group
$000/000$	$Pm\bar{3}m$
$000/0^+0^+w^+$	$P4mm$
$---/u^+u^+u^+$	$R3c$
$---/000$	$R\bar{3}c$
$00-/000$	$I4/mcm$
$--0/u^-\bar{u}^-0^-$	$Imma$

TABLE II. Correspondence between pattern notation used in the main manuscript and space group for PTO.

of Fig. (2), the antiferroelectric (AFE) displacements in the $Imma$ phase of Pb [that are, $(\delta_{Pb}, -\delta_{Pb}, 0)$] atoms and the O_3 atom $(1/2 + \delta_{O_3}, 1/2 - \delta_{O_3}, 0)$, with modulation vector $R = (1/2, 1/2, 1/2)$ in pseudocubic axes, are depicted and show increase of the AFE order with n_{ph}. Concurrently, we have plotted the tilt angle of the $a^-a^-c^0$ $Imma$ phase and $a^-a^-a^-$-tilted $R3c$ and $R\bar{3}c$ phases in $PbTiO_3$ in Fig. (3). It is clear that the tilt angle increases with n_{ph} consistent with the increased instability at the R point in the phonon band structure of the paraelectric cubic phase presented in the main manuscript.

MINIMUM ENERGY PATH

In order to discuss the metastability of the relevant phases (we restrict ourselves to the case of PTO), we performed calculations using the simplified string method within Abinit [3]. We plot the minimum energy transition path between the $P4mm$ and $Imma$ phases in Fig. (4), for which one observes that, in dark conditions (blue circles), $Imma$ is a local maximum of the energy landscape, and is therefore *unstable*. Yet, photoexcitation is able to transform that instable maxima into a local minima (see for instance gold triangle, correspond-

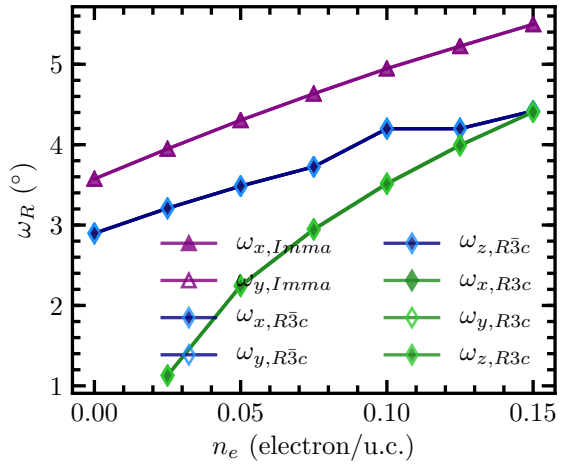

FIG. 3. Tilt angle of the oxygen octahedron in the *Imma*, *R*3*c* and $R\bar{3}c$ phases in $PbTiO_3$.

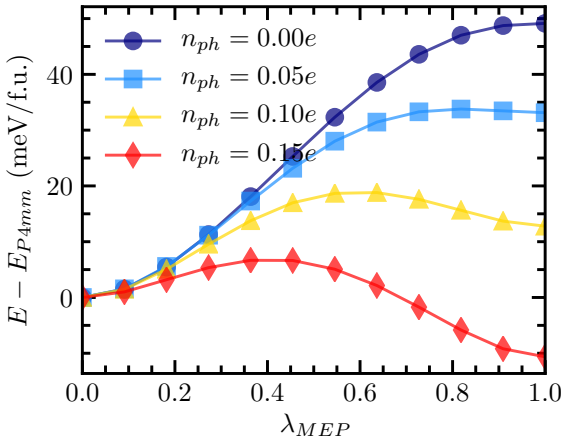

FIG. 4. Energy change along the minimum energy path (denoted by the adimensional parameter λ_{MEP}) linking the *P*4*mm* and *Imma* phases in PTO, for n_{ph} = 0.00 e/f.u. (navy circles), n_{ph} = 0.05 e/f.u. (dodgerblue squares), n_{ph} = 0.10 e/f.u. (yellow triangles) and n_{ph} = 0.15 e/f.u. (red diamonds).

ing to n_{ph} = 0.10 e/f.u., in Figure 4) , hence creating a metastable state in PTO. At larger concentration of photoexcited carriers (red diamonds in Figure 4), *Imma* even becomes stable compared to the *P*4*mm* state!

ABOUT A MONOCLINIC PHASE IN BTO

Let us discuss the presence of a monoclinic phase, in particular in BTO, that was reported experimentally both under illumination in nanowires [4] and through electron doping [5]. We attempted to construct a

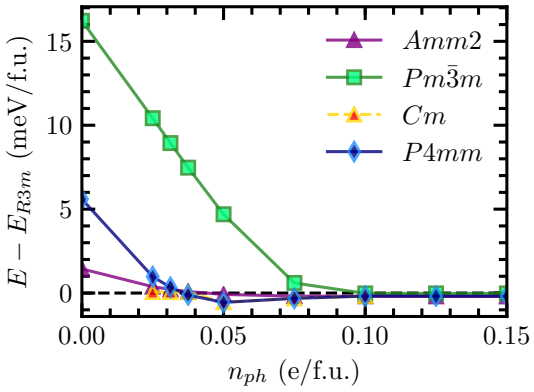

FIG. 5. Energy of different phases in BTO with respect to the $000/u^+u^+u^+$ (*R*3*m*) structure (dashed dark line), which is the ground state in the dark, including that of the attempted *Cm* structure.

monoclinic *Cm* phase, however the relaxed structure is structurally and energetically extremely close to the $000/u^+u^+u^+$ and $000/00w^+$ phase. We thus cannot conclude with certainty about the existence of a monoclinic phase as a ground state. Nonetheless, Fig. (5) shows the existence of multiple phases with different orientations of the polarization in a close energy window near n_{ph} = 0.03 e/f.u., indicating flattening of the energy landscape. We thus expect the appearance of a low symmetry phase to bridge the rhombohedral and tetragonal phases, and large electromechanical properties, as is commonly found at morphotropic phase boundaries in relaxor-ferroelectric solid solutions [6, 7].

PARALLEL WITH HYDROSTATIC PRESSURE

It is clear from Fig. (6) that most non-trivial phases (*i.e.*, other than the cubic paraelectric phase 000/000) show a *decrease* in volume when carriers are photogenerated. This is consistent with a reduction of the polar order and is also typically expected when a perovskite is subject to hydrostatic pressure. It is also interesting to note that Ref. [8] drew parallels between doping and hydrostatic pressure, and that Ref. [9] proposed that the potential-deformation mechanism could generate an effective photo-induced stress.

However, we note that

- The volume of the cubic phase of BTO *increases* (see Fig. (6.a)) with n_{ph}; the volume of the cubic phase in PTO is non-monotonous, starting to decrease at low n_{ph} and then increasing at large n_{ph} (see Fig. (6.b)).

- Looking at the many phases reported in PTO un-

der pressure [10–12] ($00-/00w^+$, $--0/u^-\bar{u}^-0^-$, monoclinic phases, $---/u^+u^+u^+$, $---/000$), we note that the most stable phases at large concentrations of photo-excited carriers are $--0/u^-\bar{u}^-0^-$ or $---/000$. In other words, while the $---/000$ phase was previously reported above 20 GPa [12], we predict here that $--0/u^-\bar{u}^-0^-$ is more stable. In addition, $00-/00w^+$ and $--0/u^-\bar{u}^-0^-$ predicted or observed in Refs. [10, 11] are not stable phases here.

It is thus doubtful that the effect presently observed can be solely described in terms of hydrostatic pressure. Nonetheless, we not that Ref. [9] identified two sources of photo-induced deformations: *(i)* photo-induced stress, mediated by the potential-deformation mechanism (in other words roughly $\propto \frac{\partial E_g}{\partial \eta}$, with η being the strain and E_g the bandgap) and *(ii)* a combined action of the converse piezoelectric effect and an effective photo-induced electric field ($\propto \frac{\partial E_g}{\partial P}$). It would thus be interesting to investigate whether the photo-induced transitions discussed here can be understood as a suitable combination of applied external stresses and electric fields.

INTERATOMIC FORCE CONSTANTS

In Figure 7, we calculate the interatomic force constants (IFCs) in $2\times2\times2$ supercells of the cubic phase in both BTO and PTO, for different concentration of photoexcited carriers, using the PHONOPY package (version 1.14.2) [13]. The IFC are defined as

$$IFC_{ij,\alpha\beta} = \frac{\partial F_{i,\alpha}}{\partial \tau_{j,\beta}} = \frac{E_{KS}}{\partial \tau_{i,\alpha}\partial \tau_{j,\beta}}, \quad (1)$$

and characterize the force felt by an atom i in direction α ($\alpha = X, Y$ or Z) when atom j is moved by an increment $\delta\tau_{j,\beta}$ in direction β. In the cubic phase, $IFC_{XX} = IFC_{YY} = IFC_{ZZ}$ and $IFC_{YZ} = IFC_{ZX} = IFC_{XY}$. We plot IFC_{XX} and IFC_{XY} for different atom pairs (*e.g.* Ti-O (first neighbors, located around 2 Å), *etc.*), which we classify by distance separating the atom pairs i and j in the supercell. It is clear in Figure 7 that for most atom pairs, the IFCs are reduced under photoexcitation, most notably the 4^{th} neighbors (located around 4 Å), and corresponding to Ti-Ti and O-O interactions. We also note that the reduction of the "long range" forces, already discussed in Ref. [8], is consistent with the destabilization of the polar phase; indeed, polar order is mainly thought to originate from long range Coulomb interaction. Note however that, in doped (hence metallic) cases, short range "metascreening" forces may represent a competing force towards the stabilization of some sort of polar order [8]. In our case, BTO is predicted to show a cubic non-polar character under large photoexcitation, which is consistent with the fact that the metascreening forces are not strong in BTO (under doping with electrons) [8]; in contrast, in PTO, although the ferroelectric instability survives in the phonon dispersion curves (most likely due to metascreening, according the calculation in Ref. [8]), it is overcome by the tilt instability (see Figures 2e-h in the main manuscript).

MANY BODY CORRECTIONS TO THE BAND GAP

Density functional theory fails to accurately describe quasi-particle excitations. In particular, it is well known that the bandgap is, in general, underestimated. Therefore, we have performed G_0W_0 [19] calculations within the plasmon-pole approximation to calculate the change in the bandgap and other modifications of the bandstructure. We have used the `Quantum Espresso` [14, 15] code for the calculation of Kohn-Sham wave functions and energies on the LDA level and then the `Yambo` [16, 17] package for the G_0W_0 corrections on the three relevant phases in $BaTiO_3$ and $PbTiO_3$. We have used an $8\times8\times8$ k-point grid in the case of the cubic phase with 5 atom per unit cell (and corresponding k-meshes on the other phases that contain more atoms in the unit cell). A 30 Ry plane wave cut-off is chosen for the exchange self-energy computation; 60 and 260 bands are selected in the computation of the independent particle polarizability χ_0 and the screening operator W, respectively.

In Tables III & IV, we present the bandgap as determined in LDA and from G_0W_0 for the three relevant BTO and PTO phases. We note that the use of many-body techniques mostly shifts rigidly the conduction band up, as for example shown in the case of PTO $000/00w^+$ in Fig. 8. The bandgap correction is slightly different for the different phases, but the maximum variation is 90 meV for BTO and 140 meV for PTO. The correction is smallest for the non-polar phase, which further strengthens the result that non-polar phases are favored under illumination. Although the concentration of electrons needed to actually perform the photo-induced transition will be altered, we conclude that it will not alter the realization of such transition. If anything, at least in BTO, it should actually lower the number of photoexcited carriers necessary to reach the transition. In addition, our phonon dispersion calculations (Fig. 2 of the main text) do reveal that the cubic phase tends to be stabilized in $BaTiO_3$, while in $PbTiO_3$ antiferrodistortive phases tend to be stabilized.

Since the GW method is not a total energy method, one cannot perform a structure relaxation with it. In order to do so, one would need to perform a total energy calculation in the optically excited state either with an approach using the Bethe-Salpeter extended to a high density of excitons or with a total energy calculation on

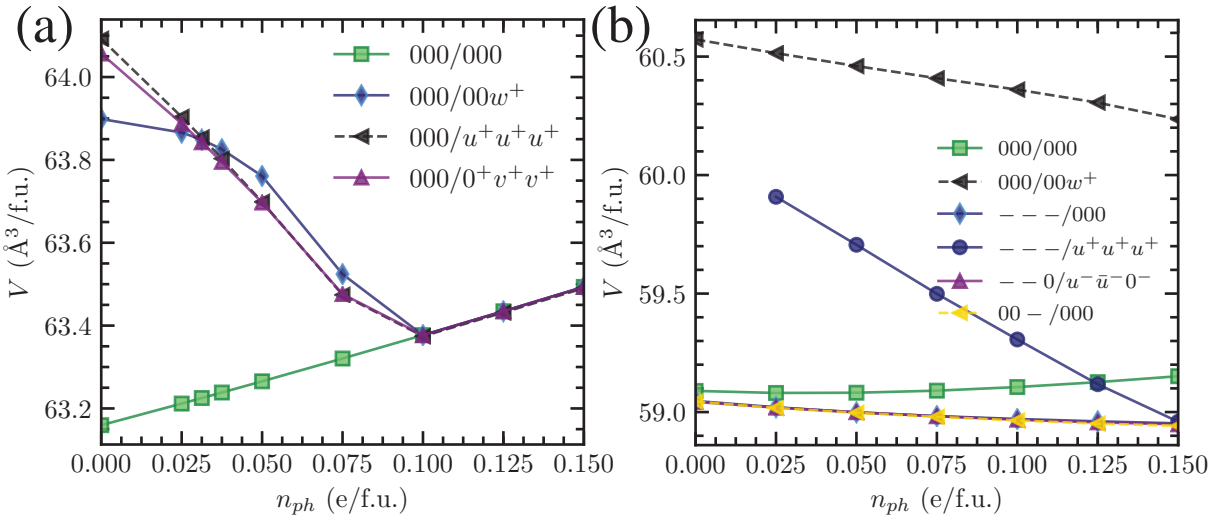

FIG. 6. Volume change of the 5-atom perovskite cell with concentration of photo-excited carriers n_{ph} in (a) BTO and (b) PTO.

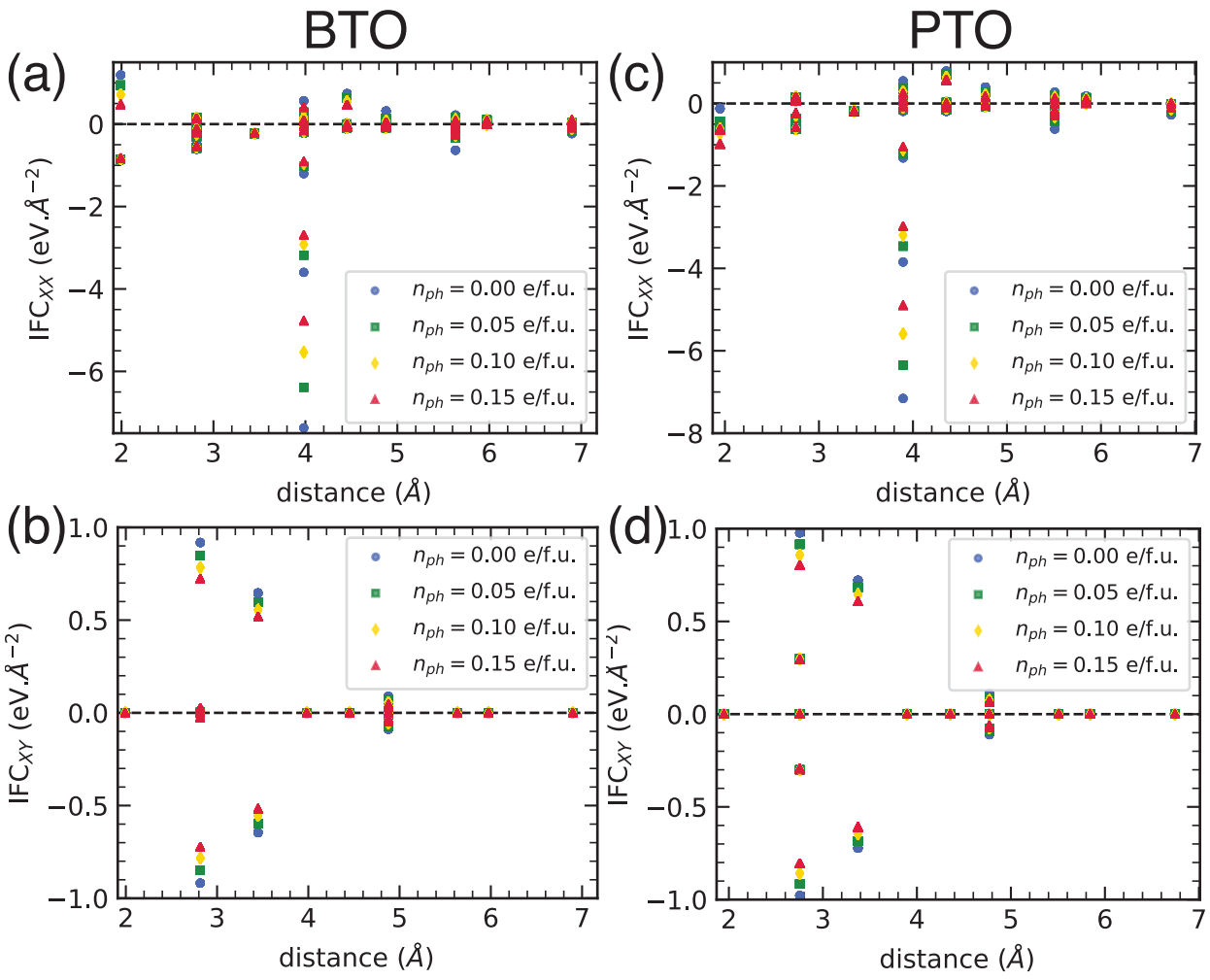

FIG. 7. Interatomic Force Constants (IFCs) in the cubic phase for XX and XY components for BTO (a & b) and PTO (c & d) for photoexcited carrier concentrations n_{ph} = 0.00 (blue circles), 0.05 (green square), 0.10 (gold diamond) and 0.15 e/f.u. (red triangle).

Phase	$E_{g,LDA}^{indirect}/E_{g,LDA}^{direct}$ (eV)	$E_{g,PBESol}^{indirect}/E_{g,PBESol}^{direct}$ (eV)	$E_{g,G_0W_0}^{indirect}/E_{g,G_0W_0}^{direct}$ (eV)	$\delta E_g^{indirect}/\delta E_g^{direct}$ (eV)
000/000	1.813/1.893	1.781/1.904	3.362/3.477	+1.549/+1.584
$000/00w^+$	1.833/2.109	1.817/2.225	3.437/3.725	+1.604/+1.616
$000/u^+u^+u^+$	2.130/2.359	2.286/2.634	3.769/4.014	+1.639/+1.655

TABLE III. Indirect and direct bandgap in $BaTiO_3$ using the *LDA* approximation for the exchange-correlation energy, and G_0W_0 corrections to take into account the many-body effects. The difference of bandgaps between the G_0W_0 and *LDA* approximations are shown in the last column.

Phase	$E_{g,LDA}^{indirect}/E_{g,LDA}^{direct}$ (eV)	$E_{g,G_0W_0}^{indirect}/E_{g,G_0W_0}^{direct}$ (eV)	$\delta E_g^{indirect}/\delta E_g^{direct}$ (eV)
000/000	1.539/1.550	3.000/3.007	+1.461/+1.457
$000/00w^+$	1.589/1.888	3.192/3.527	+1.603/+1.639

TABLE IV. Indirect and direct bandgap in $PbTiO_3$ using the *LDA* approximation for the exchange-correlation energy, and G_0W_0 corrections to take into account the many-body effects. The difference of bandgaps between the G_0W_0 and *LDA* approximations are shown in the last column.

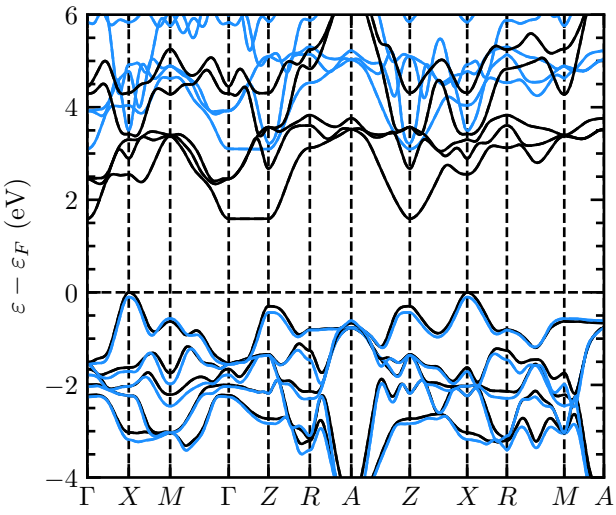

FIG. 8. *LDA* (black) and G_0W_0 (light blue) corrected band structure of $000/00w^+$ PTO.

the level of the random-phase approximation for an excited carrier occupation. Both are currently out of reach. However, the use of hybrid functionals within DFT allows to take approximately those effects into account. Calculations are presented in the following section.

Furthermore, it is worth noting that, from time-resolved pump-probe experiments, the exciton lifetime is in general considered to be close to the picosecond because of inelastic scattering by phonons [18]. This is rather large compared to the radiative recombination lifetime which is considered larger than a nanosecond [18]. As a result, one expects in a stationary regime that a large amount of photoexcited carriers are free band carriers and follow a quasi-Fermi-Dirac distribution; only a small fraction of the photoexcited carriers will be non-thermalized.

CALCULATIONS OF THE SOFT MODE STABILIZATION WITH HYBRID FUNCTIONALS

In order to test the robustness of our results on the stabilization of the soft mode in BTO upon charge excitation, we have also performed calculations using hybrid functionals that combine semi-local exchange-correlation energy with a fraction of exact Hartree-Fock exchange. Since calculations with hybrid functionals are more efficient when using localized basis sets, we have used the code `CRYSTAL`[21] for this purpose. We have used the Gaussian basis sets of Ref. 22 which are optimized for BTO. The code does not foresee calculations with separate quasi-Fermi levels of excited electrons and holes. Therefore, we have used a simple Fermi-Dirac smearing (with exaggerated high temperatures) in order to promote electrons from the valence band top to the conduction band minimum. The excited charge density can then be easily calculated from the occupation numbers of the excited bands. Fig. 9 demonstrates that the result is qualitatively the same as for the quasi-Fermi-Dirac distribution. We have performed calculations with the semi-local PBEsol functional (which yields - with the given basis set - an optimized lattice parameter of 3.989 Å and a band gap of 2 eV) and calculations using the hybrid HSEsol functional[20] (which yields an optimized lattice constant of 3.966 Å and a band gap of 3.4 eV, close to the value of the GW band gap). Due to the difference in lattice constants and functionals, the exact values of the phonon modes in PBEsol and HSEsol are slightly different, but they display the same behaviour as a function of the excited charge density for both functionals. The modes with positive frequencies are remarkably stable under charge excitation. However, the polar soft phonon

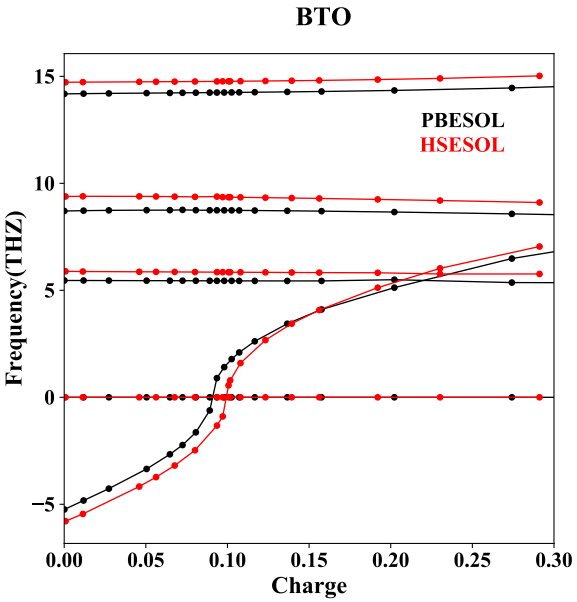

FIG. 9. Phonon frequencies of the cubic phase of BTO as a function of excited charge density (in electron/formula unit). We compare calculations performed with the semi-local PBEsol functional (black lines) and with the hybrid HSEsol functional (red lines).

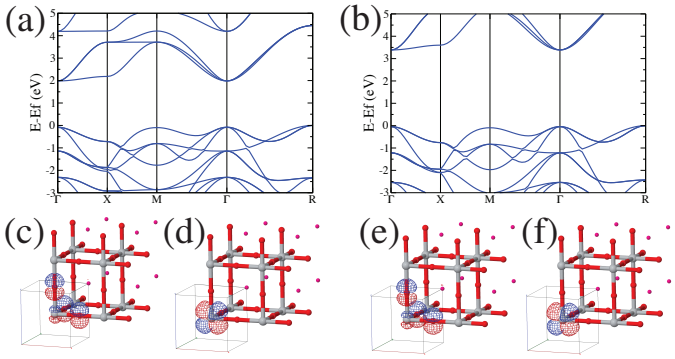

FIG. 10. Band structures of cubic 000/000 BTO calculated using the (a) PBESol and (b) HSESol functionals with the CRYSTAL code. The isosurfaces of the wavefunctions corresponding to the top of the valence band (c & e) and the bottom of the conduction band (d & f) are depicted for the PBESol and HSESol functionals respectively.

mode is strongly influenced. At low excited charge density it has negative (or, more precisely, imaginary) frequency. At an excited charge density of 0.09 – 0.1 electron per formula unit, it is stabilized and converges towards an optical frequency at high charging. This behaviour is qualitatively and semi-quantitatively the same for both functionals and it is consistent with the phonon dispersion in Fig. 2 of the main manuscript. The calculations thus demonstrate that the stabilization mechanism is robust under changes in the band gap (as mimicked by different functionals) and under changes in the details of the excited states occupation (e.g., Fermi-Dirac distribution versus distribution with separate quasi-Fermi levels). Note that for the HSEsol functional the crossover is at slightly larger excited charge density than for the PBEsol functional. This may be considered to be in contrast to our remark that the GW corrections seem to favor the stability of the cubic phase. Note, however, that the HSEsol functional (and its corresponding lattice optimization) leads to an increase of the lattice instability (reflected in the larger absolute value of the imaginary frequency) and thus needs a larger excited charge density in order to overcome this instability.

In addition, in Figs. 10a-b, we compare the band structures obtained for cubic BTO with the PBESol and the HSESol exchange-correlation functionals. Apart from a rigid upshift of the conduction bands of the HSESol band structure, the band dispersions are similar across the two functionals. Furthermore, we further report the amplitude of the states at the top of the valence band in Fig. 10c and bottom of the conduction band in Fig. 10d for the PBESol functional in cubic BTO. Similar data are given in Figs. 10e and 10f but for the HSESol functional. No change in the atomic character of those states can be observed between those two functionals.

INFLUENCE OF THE EXCHANGE-CORRELATION FUNCTIONAL

We also tested the influence of the functional on the phonon dispersions and the total energy in the special case of $BaTiO_3$. The main manuscript uses the PBESol functional as it gives an overall rhombohedral ground state structure which is closer to experiments than LDA. Indeed, our lattice constants in the rhombohedral phase of BTO in the electronic ground state are 3.963 Å and 89.927° in LDA, 4.002 Å and 89.868° in PBESol, while low temperature structural characterization experiments show lattice constants of 4.004 Å and 89.839° in Ref. [2]. However, LDA calculations show qualitative agreement with the results obtained using the PBESol functional, as shown in Figs. 11 & 12.

* charles.paillard@centralesupelec.fr

[1] H. D. Megaw, *Acta Crystallographica* **5**, 739 (1952).
[2] G. H. Kwei, A. C. Lawson, S. J. L. Billinge, S. W. Cheong, *The Journal of Physical Chemistry* **97**, 2368 (1993).
[3] E. Weinan, W. Ren, E. Vanden-Eijnden, *J. Chem. Phys.* **126**, 164103 (2007).
[4] Y.-H. Kuo, S. Nah, K. He, T. Hu, A. M. Lindenberg, *Journal of Material Chemistry C* **5**, 1522 (2017).
[5] J. Fujioka, *Scientific Reports* **5**, 13207 (2015).

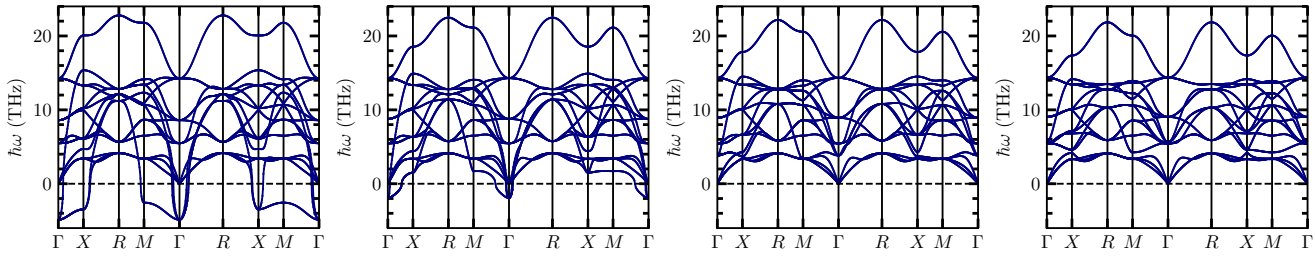

FIG. 11. Phonon spectra of the cubic paraelectric high-symmetry phase of BTO using the LDA exchange-correlation functional, for different excited carrier concentrations: from left to right, $n_{ph} = 0$, 0.05, 0.10 and 0.15 e/f.u.

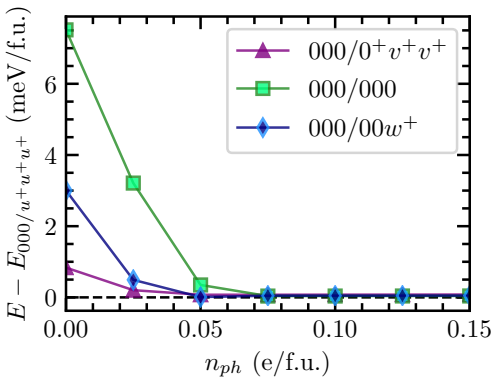

FIG. 12. Kohn-Sham energy of various phases in BTO using the LDA functional.

[6] Z.-G. Ye, B. Noheda, M. Dong, D. E¿ Cox, G. Shirane, *Physical Review B* **64**, 184114 (2001).

[7] L. Bellaiche, A. García, D. Vanderbilt, *Physical Review Letters* **84**, 5427 (2000).

[8] H. J. Zhao *et al. Physical Review B* **97**, 054107 (2018).

[9] C. Paillard, S. Prosandeev, L. Bellaiche, *Physical Review B* **96**, 045205 (2017).

[10] I. A. Kornev, et al. *Physical Review Letters* **95**, 196804 (2005).

[11] P.-E. Janolin, *et al. Physical Review Letters* **101**, 237601 (2008).

[12] M. Ahart, *et al. Nature* **451**, 545 (2008).

[13] A. Togo, I. Tanaka, *Scripta Materialia* **108**, 1 (2015).

[14] P. Giannozzi, *et al. J. Phys. Condens. Matter* **21**, 395502 (2009).

[15] P. Giannozzi, *et al. J. Phys. Condens. Matter* **29**, 465901 (2017).

[16] A. Marini, C. Hogan, M. Grüning, D. Varsano *Comput. Phys. Commun.* **180**, 1392–1403 (2009).

[17] D. Sangalli, A. Ferretti, H. Miranda, C. Attaccalite, I. Marri, E. Cannuccia, P. Melo, M. Marsili, F. Paleari, A. Marrazzo, G. Prandini, P. Bonfà, M.O. Atambo, F. Affinito, M. Palummo, A. Molina-Sánchez, C. Hogan, M. Grüning, D. Varsano, A. Marini, arXiv:1902.03837 [cond-mat.mtrl-sci] (2019).

[18] C. Thomsen, H.T. Grahn, H.J. Maris, and J. Tauc, *Phys. Rev. B* **34**, 4129 (1986).

[19] M. S. Hybertsen, S. G. Louie, *Phys. Rev. B* **34**, 5390 (1986).

[20] L. Schimka, J. Harl, and G. Kresse, *J. Chem. Phys.* **134**, 024116 (2011).

[21] R. Dovesi, A. Erba, R. Orlando, C. M. Zicovich-Wilson, B. Civalleri, L. Maschio, M. Rerat, S. Casassa, J. Baima, S. Salustro, B. Kirtman, *WIREs Comput Mol Sci.* **8**, e1360 (2018)

[22] G. Sophia, P. Baranek, C. Sarrazin, M. Rerat, R. Dovesi, *Phase Transitions: A Multinational Journal*, **81**, 1069-1084 (2013).